Acta Biomaterialia 54 (2017) 386–398

Contents lists available at ScienceDirect

Acta Biomaterialia

journal homepage: www.elsevier.com/locate/actabiomat

Full length article

Surface-enrichment with hydroxyapatite nanoparticles in stereolithography-fabricated composite polymer scaffolds promotes bone repair

O. Guillaume [a], M.A. Geven [b], C.M. Sprecher [a], V.A. Stadelmann [a], D.W. Grijpma [b], T.T. Tang [c], L. Qin [d], Y. Lai [d], M. Alini [a], J.D. de Bruijn [e], H. Yuan [e], R.G. Richards [a], D. Eglin [a,*]

[a] AO Research Institute Davos, Clavadelerstrasse 8, CH 7270 Davos, Switzerland
[b] MIRA Institute for Biomedical Engineering and Technical Medicine, Department of Biomaterials Science and Technology, University of Twente, P.O. Box 217, 7500 AE Enschede, The Netherlands
[c] Shanghai Key Laboratory of Orthopedic Implants, Department of Orthopedic Surgery, Shanghai Ninth People's Hospital, Shanghai Jiao Tong University School of Medicine, Shanghai, China
[d] Translational Medicine Research and Development Centre, Institute of Biomedical and Health Engineering, Shenzhen Institute of Advanced Technology, The Chinese Academy of Sciences, Shenzhen, China
[e] Xpand Biotechnology BV, Professor Bronkhorstlaan 10-d, 3723 MB Bilthoven, The Netherlands

ARTICLE INFO

Article history:
Received 1 December 2016
Received in revised form 2 March 2017
Accepted 6 March 2017
Available online 7 March 2017

Keywords:
Surface-enrichment
Hydroxyapatite nanoparticles
Poly(trimethylene carbonate)
Stereolithography
Osteoconductive scaffold
Bone regeneration

ABSTRACT

Fabrication of composite scaffolds using stereolithography (SLA) for bone tissue engineering has shown great promises. However, in order to trigger effective bone formation and implant integration, exogenous growth factors are commonly combined to scaffold materials. In this study, we fabricated biodegradable composite scaffolds using SLA and endowed them with osteopromotive properties in the absence of biologics. First we prepared photo-crosslinkable poly(trimethylene carbonate) (PTMC) resins containing 20 and 40 wt% of hydroxyapatite (HA) nanoparticles and fabricated scaffolds with controlled macro-architecture. Then, we conducted experiments to investigate how the incorporation of HA in photo-crosslinked PTMC matrices improved human bone marrow stem cells osteogenic differentiation *in vitro* and kinetic of bone healing *in vivo*. We observed that bone regeneration was significantly improved using composite scaffolds containing as low as 20 wt% of HA, along with difference in terms of osteogenesis and degree of implant osseointegration. Further investigations revealed that SLA process was responsible for the formation of a rich microscale layer of HA corralling scaffolds. To summarize, this work is of substantial importance as it shows how the fabrication of hierarchical biomaterials via surface-enrichment of functional HA nanoparticles in composite polymer stereolithographic structures could impact *in vitro* and *in vivo* osteogenesis.

Statement of Significance

This study reports for the first time the enhance osteopromotion of composite biomaterials, with controlled macro-architecture and microscale distribution of hydroxyapatite particles, manufactured by stereolithography. In this process, the hydroxyapatite particles are not only embedded into an erodible polymer matrix, as reported so far in the literature, but concentrated at the surface of the structures. This leads to robust *in vivo* bone formation at low concentration of hydroxyapatite. The reported 3D self-corralling composite architecture provides significant opportunities to develop functional biomaterials for bone repair and tissue engineering.

1. Introduction

Bone is the most frequently transplanted tissue after blood, and the need for effective and patient specific bone graft substitute materials, supplanting autografts and allografts, remains enormous

* Corresponding author.
E-mail address: david.eglin@aofoundation.org (D. Eglin).

http://dx.doi.org/10.1016/j.actbio.2017.03.006
1742-7061/

[1]. Additive manufacturing (AM) technologies have emerged as promising alternatives to classical fabrication processes for bone repair materials based on patient's specific information [2]. Among AM techniques, stereolithography (SLA) was one of the first introduced, three decades ago by Chuck Hull, as a system "*able to generate 3D objects from a fluid medium by step-wise and successive alteration through specific stimulation*" [3] and is still nowadays nourishing major innovations. Indeed, SLA has shown great interest in the field of tissue repair due to the high geometric resolution achieved [4], which remains extremely challenging to approach with other AM technologies, especially when considering the layer-by-layer fabrication of calcium phosphate (CaP)-containing biomaterials.

SLA technique brings tremendous advantages in terms of control of the internal macro/micro-architecture, of the degree of porosity and organization of the pores and, more importantly, in terms of freedom regarding the customized composition, design and shape of the fabricated biomaterial implants [2]. More specifically for bone repair purposes, an overview of the polymer/CaP composite structures fabricated so far using SLA indicated that, mostly biodegradable polyesters resins with a dispersion of micro- and nanoparticles of CaP ceramic (as high as 60 wt%) have been proposed (Supplementary Table 1). From the presented list, it is clear that the most widely employed biodegradable polymers are represented by the family of the polyesters. Nevertheless, a new biodegradable and biocompatible polycarbonate polymer (*i.e.* poly(trimethylene carbonate), PTMC) has just been introduced to this specific biomedical field of application [5,6]. Exploratory investigations revealed that PTMC-based biomaterials exhibit unique and versatile features, regarding numerous parameters (such as the kinetic and the mechanism of resorption, the mechanical properties, the chemical functionalizations, *etc.*) compared to common alternatives such as biodegradable aliphatic polyesters (including poly(lactic acid) (PLA), poly(glycolic acid) (PGA) or poly(ε-caprolactone) (PCL)) [7].

As instance, for all these synthetic biodegradable polyesters, the degradation mechanism is relatively similar, driven by hydrolysis of the ester linkages, releasing acid by-products [8], which can cause inflammatory reaction, upon local acidic oligomers accumulation, and exacerbate fibrotic reaction and bone resorption [9,10]. In opposition to the hydrolytic degradation of the above-mentioned polyesters, PTMC degradation is in majority driven by enzyme and oxidative species via a surface erosion mechanism [11]. Additionally, the structural mechanical integrity of the PTMC tends to be better maintained overtime attributed to this singular erosion mechanism [7,12,13]. Fabrication of PTMC scaffolds using SLA has already been widely investigated, but without focusing on bone tissue repair yet. We hypothesized that SLA-fabricated composite PTMC scaffolds could exhibit advantageous features compared to the available biomaterials presented ST 1.

Noteworthy, none of the reported composite microstructures fabricated by stereolithography promoted significant bone formation *in vivo* in the absence of additive factors, such as BMP-2 [14,15]. One of the reasons is that the main composite scaffolds are constituted of inorganic CaP particles physically entrapped in photo-crosslinked polymeric matrices. We postulated that the restricted exposition of CaP to the external environment combined with inadequate degradation kinetic of composite SLA-scaffolds, hinder effective bone healing capacity [16]. Controlling spatial arrangement of CaP particles inside 3D printed scaffolds could alleviate this limitation. Interestingly, organized nano/microscale assemblies of loaded nanoparticles in polymer composites have been investigated in the field of electronic, optic, photovoltaic and self-healing materials [17,18]. Such nano/microscale particle arrangements are actually dictated by the size and radius, the shape, the volume fraction and importantly, the surface interaction between the nanoparticles and the polymer matrix [19]. As a result, disparate nanoparticles in a polymer mixture can self-organize at the interface of immiscible solvents and polymer blends that leads to hierarchically structured composites [17]. Controlling this spatial segregation has been achieved in extrusion and solvent casting processes [20], but interestingly not exploited yet in 3D printing and stereolithography manufacturing.

In this study, using *in vitro* and *in vivo* experiments, we first deciphered how the developed SLA-PTMC/HA composite structures commanded osteogenesis and drove the bone healing cascade. Topographical analyses performed on the scaffolds revealed that stereolithography processing resulted in a surface-enrichment with agglomerated HA nanoparticles at the surface interface of the disparate PTMC/HA scaffold. This investigation is of great importance as it paves the way for further optimizations regarding the modulation of nanoparticles spatial arrangement in 3D-printed structures.

2. Experimental section

2.1. Preparation of photo-crosslinked PTMC/HA composite macroporous scaffolds

Three-armed poly(trimethylene carbonate) (PTMC) was synthesized by ring-opening polymerization of trimethylene carbonate with trimethylolpropane using $Sn(Oct)_2$ as catalyst [5,6]. A PTMC macromer with methacrylate end-groups (PTMC-MA) was subsequently prepared by reacting PTMC hydroxyl groups with methacrylic anhydride [6]. Different resin formulations were prepared with a varying content of nano-hydroxyapatite (HA). Xpand Biotechnology BV (Bilthoven, The Netherlands) kindly provided HA in the form of a powder with aggregates (Ø = 15 μm) of needle-like HA crystals of 200 to 400 nm long and 20 to 50 nm wide. Those nano-HA particles were prepared using a wet-precipitation technique [21]. A stoichiometric Ca/P ratio of 1.67 was selected to produce the needle-like HA particles, similar to the mineral composition and shape of HA in human bone.

First, PTMC-MA and HA were dispersed in chloroform and precipitated in cold methanol. The resulting dried PTMC-MA/HA powder was mixed with propylene carbonate diluent (Merck Millipore), Lucirin® TPO-L photo-initiator (BASF) and Orasol Orange G dye (from Ciba Speciality Chemicals).

From the resins, scaffolds (6 × 3.5 mm, diameter × height) with gyroid porosity were fabricated using an Envisiontec Perfactory$^{3®}$ SXGA^{+} Standard UV stereolithography system. A light intensity of 180 mW/dm^2 was used with an irradiation time of 9 seconds per layer and the platform was elevated by 50 μm between each layer. The internal architecture parameters of the manufactured scaffolds were designed suitable to allow for vascularisation and bone ingrowth/formation [22], with minimal pore size of 600 μm, porosity of 70% and interconnectivity 100%. Following materials fabrication, propylene carbonate diluent was removed by extraction in propylene carbonate/ethanol (1/1 v/v), gradually exchanged to 100% ethanol, the scaffolds were then dried and sterilized using cold ethylene oxide gas procedure.

For the experiments performed on 2D surfaces, films were prepared by solvent casting of the resins on glass plates and subsequent photo-crosslinking in a UV-crosslinking box at 365 nm and 1100 mW/dm^2 for 5 min under N_2. Following fabrication, films' purification and sterilization were performed the same way as previously described for porous scaffolds.

2.2. Materials characterization

The architecture of the scaffolds was analysed by Scanning Electron Microscopy (SEM, refer to Section 2.3.1.) and micro-computed

tomography (microCT). Briefly, the volume fraction of porosity, the trabecular thickness and trabecular space were measured (corresponding to the strut and pore diameters respectively) using bone trabecular morphometry script (n = 3, with a microCT 40; 30 μm voxel size, SCANCO Medical AG, Bruettisellen, Switzerland). Additionally, HA particles repartition in the trabecular structure of the porous scaffolds was observed using a high-resolution microCT scanner (microCT 100; 3 μm voxel size).

Calcium ions released from the scaffolds (weighing 45 ± 2 mg) immersed in phosphate saline buffer (PBS) at 37 °C (1 mL) was assessed. At day 1, 3, 4, 7, 12, 19 and 28, the supernatant was removed and replaced by fresh PBS. The quantification of calcium in the supernatant was performed via the formation of chromogenic reagent by complexation of Ca^{2+} with o-cresolphthalein (Calcium Colorimetric Assay Kit, Sigma-Aldrich) measured at 560 nm (n = 3 per group).

Protein adsorption was investigated by incubating scaffolds in PBS containing 10% of Serum (SeraPlus, Milan Analytica, Basel, Switzerland), at 37 °C for 5 days, using Quick Start™ Bradford protein kit (Bio-Rad Laboratories, Cressier, Switzerland), according to the manufacturer's protocol using bovine serum albumin (BSA) as standard (n = 3 per group).

Swelling/shrinkage was estimated by incubating scaffolds for 28 days in sterile PBS and conducting microtomography scans (using microCT 40) of the same scaffold before and after drying (48 h at 40 °C under vacuum at 200 mbar). Swelling quantification was expressed in percentage of the trabecular thickness (Tr. Th.) of the scaffold (n = 3 per group) and calculated using the Eq. (1).

$$Swelling\ (\%) = Tr.Th\frac{wet - dry}{wet} * 100. \quad (1)$$

Additionally, the wettability of the different surfaces was characterized using the contact angle method on films (Drop Shape Analysis System, DSA10 Krüss, Germany, n = 10 per group).

2.3. In vitro investigation

Human bone marrow mesenchymal stem cells (hBMSCs) were isolated from vertebral body bone marrow aspirates (obtained from donors undergoing spinal fusion with informed consent and full ethical approval (KEK Bern 126/03)). hBMSCs of two donors were expanded individually [23] and used separately (at passage 3) for the following experiments, but all the values were finally pooled in the presented histograms.

2.3.1. In vitro investigation of scaffolds colonization and matrix deposition

SLA-fabricated scaffolds were incubated overnight in complete osteogenic medium (OM) (based on basic low glucose DMEM (GIBCO) supplemented with 10% serum (SeraPlus), 50 μg/mL ascorbic acid, 10 nM dexamethasone and 5 mM glycerol-2-phosphate (all from Sigma-Aldrich)), before seeding with 150 μL of a cell suspension containing 1×10^6 hBMSCs/mL.

After 8 h, the seeded scaffolds were moved to a new low-adhering 24 well-plate (Nunclon Sphera, ThermoFisher Scientific, Zürich) in order to prevent cells to proliferate on the bottom of the plate, and incubated with OM (1 mL per well, changed three times a week). 24 h and 28 days post-seeding, samples were rinsed with PBS and subjected to various analyses.

Cell viability was evaluated with Live/Dead® staining. The samples were incubated with calcein acetoxymethylester and ethidium homodimer, at 10 and 1 μg/mL respectively, washed and imaged using fluorescent confocal microscope (Axiovert 200 m microscope equipped with an AxiocamHRc and Axiovision software (Zeiss, Gottingen, Germany)).

SEM analysis was performed after fixation in buffered paraformaldehyde at 4%, followed by gradual dehydration in ethanol and by immersion in hexamethyldisilazane (Sigma-Aldrich). After drying, the samples were sputter-coated with Au-Pd and investigated by electron microscopy using a Hitachi S4700 FESEM (Hitachi, Japan). Meanwhile, the chemical composition of the scaffolds was determined by energy dispersive X-ray (EDX, Oxford Instruments, UK), following C coating.

The amount of DNA present in samples was quantified following samples digestion in proteinase K solution at 0.5 mg/mL (Roche, Mannheim, Germany) for 16 h at 56 °C, and reaction using fluorescent Bisbenzimide Hoechst 33258 at an excitation of 360 nm and an emission of 465 nm (n = 3 per group).

Collagen deposition was evaluated following specimen fixation in methanol 70%, incubation in PBS containing 5% sucrose (w/v) and immersion in cryo-compound (Tissue freezing Medium from Leica Biosystems, Muttenz, Switzerland) before cryosection (section of 8 μm, Cryostat-Microtome HM 500 OM from Carl-Zeiss, Zürich, Switzerland). Safranin-O Fast Green staining (counterstained with Weigert's Haematoxylin) was realized on cryosections (n = 2 per group).

2.3.2. hBMSCs osteogenic differentiation on PTMC/HA

hBMSCs were seeded on the different material films (6 mm Ø) at 20×10^3 cells/cm^2 and incubated in complete osteogenic medium (OM) for 4 weeks (in 96 well-plate using 100 μL of medium per well, changed three time a week), using Tissue Culture Polystyrene (TCPS) as control. As the films covered firmly the entire bottom surface of the well plate, preventing cells to proliferate on the underlying TCPS, no exchange to new well plate was performed post-seeding as it was reported for 3D scaffolds (Section 2.3.1).

For DNA quantification, samples were first incubated in lysis buffer made of Triton X-100 at 0.1% in 10 mM of Tris-HCl, pH = 7.4 (all from Sigma-Aldrich) and followed by one freezing-thawing cycle. Then, DNA amount was estimated using fluorescent CyQuant® GR Dye assay, according to the supplier's recommendation (Invitrogen), (n = 3 per group). Alkaline phosphatase activity (ALP) from the cell-lysis solution was determined using colorimetric quantification. Briefly, samples along with a set of standard solutions (*p*-nitrophenol of concentrations from 0 to 1000 μM) were incubated with alkaline buffer solution (2-amino-2-methylpropanol 1.5 M pH = 10.3, from Sigma-Aldrich) and then ALP substrate buffer was added (phosphatase substrate dissolved in diethanolamine buffer at 1 M in 0.5 mM $MgCl_2$ adjusted pH = 9.8). After mixing, and heating (at 37 °C for exactly 15 min), a solution of NaOH at 0.1 M was added to each tube in order to stop the reaction. Then, the intensity of *p*-nitrophenol formation was monitored at 405 nm. The total ALP contents were expressed as enzyme activity units in nmol/min (n = 3 per group), as a function of total DNA (ng) per well measured using CyQuant® assay.

Presence of mineralization was detected using Alizarin Red Staining assay (ARS, Sigma-Aldrich), with Thermanox plastic coverslips (NUNC™ Thermanox™ Coverslips, from ThermoFisher) used as control films (for macroscopic and SEM observations). The cell monolayer was washed with PBS, fixed with formaldehyde 4% and further washed with deionised (DI) water. Then, 40 mM ARS solution at pH = 4.2 was added to each well for 1 h and thoroughly washed with DI water for 5 days. Finally, samples were imaged by light microscopy (Macrofluo™ from Leica) and a quantification of the ARS was performed by acid extraction thereafter. Briefly, acetic acid (at 10%) was added to each well for 30 min, and the loosely attached monolayer of cells was transferred to Eppendorf tubes and heated up to 85 °C for 10 min, then placed on ice for 5 min. After centrifugation at 20,000*g* for 15 min, ammonium hydroxide was added to the supernatant (final pH of 4.1–4.5) and absorbance

was recorded at 405 nm and compared to ARS standard solutions ranged from 0 up to 2000 μM (n = 3 per group) (ARS intensities in cell-free condition at day 1 and 28 are shown as controls).

Additionally, to analyse the effect of the incorporation of HA into the PTMC matrix on the osteogenic gene expression (collagen type I (h-Col 1) and h-ALP), 3×10^5 hBMSCs were seeded on the different scaffolds and cultivated for 14 days in basal and osteogenic media (BM and OM respectively). BM contained only α-MEM supplemented with 10% of SeraPlus and OM composition was previously described (Section 2.3.1). Total RNA was isolated from TRI Reagent (Molecular Research Center, MRC) containing Polyacryl Carrier™ (at 2 μL/mL) according to the manufacturer's protocol, and the RNA was controlled qualitatively and quantitatively by spectrophotometry. 1000 ng of RNA was used for cDNA synthesis using TaqMan Reverse Transcription reagents (from Applied Biosystems) and loaded in a Thermocycler (GeneAmp 5700SDS instrument). PCR was performed on a QuantStudio™ 6 Flex Real-Time PCR System using TaqMan universal Master Mix reagents. Fold induction calculated using the ΔCT method after normalization with Fast 18S as a housekeeping gene and relative to cells grown on PTMC scaffold (without HA) in BM condition (n = 3 per condition and per donor).

2.4. Animal model experiment

2.4.1. Operative procedure and surgical implantation

Calvarial defect on rabbits (n = 8, specific pathogen free, New Zeeland-White rabbit, female, skeletally mature > 24 weeks, 4.0 ± 0.3 kg from Charles River Laboratory) was conducted following the approval of the ethical committee of the canton of Grisons in Switzerland (GR 19A/2015). All procedures were performed in an AAALAC International (Association for Assessment and Accreditation of Laboratory Animal Care) approved facility and according to Swiss animal protection law and regulations. Animals were sedated with 0.2 mg/kg Medetomidim (Domitor®, Pfizer, Switzerland), 0.2 mg/kg Midazolam (Dormicum®, Roche Pharma AG; Switzerland) and 0.005 mg/kg Fentanyl (Sintenyl®, Sintetica SA, Switzerland) intramuscularly. General anaesthesia was induced with Propofol (Propofol® 1% Fresenius, Fresenius Kabi AG, Switzerland) intravenously and animals were intubated and maintained at 1.5 to 2% Isoflurane (Isofluran Baxter®, Baxter AG, Switzerland) in oxygen. 4 mg/kg Carprofene (Rimadyl®, Pfizer AG, Switzerland) intravenously was used as preemptive analgesia together with 2–3 mg/kg ropivacaine applied locally.

After incision made from the nasal bone to the occipital crest and reflection of the soft tissue, the parietal bones were exposed. Four evenly distributed 6 mm diameter defects (non-critical size) were created with a Codman perforator apparatus (commercialized by Depuy-Synthes). The created defects were randomly assigned to 4 different groups, including empty defects (negative controls) and defects press-fitted with different PTMC/HA composites and the skin was closed with a continuous pattern of Monocryl 3.0.

Post-operative analgesia was administered to the animals (Carprofen 4 mg/kg s.c. q 24 h for 72 h; buprenorphine 0.1 mg/kg i.m. 8 h for 24 h and Fentanyl transdermal patches 12 μg/h for 72 h) and they were kept single in a cage for the entire study. MicroCT scanning of every animal was performed under general anaesthesia (as described above) postoperatively (day 0), after 3 weeks and after euthanasia (6 weeks), using a high-resolution peripheral quantitative computed tomography (HR-pQCT) operated at 59 kVp/900 μA with a nominal resolution of 82 μm (SCANCO Medical AG). Injection of fluorochromes was performed in order to observe new bone formation, by injecting calcein green and xylenol orange after 2 and 4 weeks of surgery respectively. Euthanasia of the animals was realized after 6 weeks by intravascular injection of 600 mg Pentobarbital.

2.4.2. Histology and histomorphometric evaluation

Following euthanasia, the calvaria including the four defects, without soft tissues, was resected from the skull and stored in methanol 70% for histology analyses. Undecalcified sections were obtained after methylmethacrylate embedding and stained using Giemsa-Eosin. Histomorphometric evaluation and semi-quantitative analyses were conducted by an anatomopathologist, blinded, taking into consideration the inflammatory response, the osteotomy content (nature and composition of the neo-formed tissue), the vascularization and the osseointegration of the scaffolds.

2.5. Statistical analyses

Statistical analysis of data was performed using Prism software (GraphPad Software, La Jolla, CA, USA). We assumed normal distribution of data. One way ANOVA with Tukey's multiple comparison test was applied to detect significant differences between experimental groups (with $p < 0.05$). Data presented are means ± standard deviation (SD) unless stated otherwise.

3. Results

3.1. Fabrication and characterization of disparate PTMC/HA scaffolds

Resins (see Supplementary Table 2 for description of the formulations) were optimized for fabrication of scaffolds of photo-crosslinked PTMC and disparate PTMC/HA using stereolithography technique (SLA). Composite scaffolds of PTMC combined with 0, 20 and 40 wt%. HA, labelled respectively as PTMC, PTMC 20 and PTMC 40, were SLA-fabricated.

Macroscopically, the SLA-fabricated scaffolds resembled the designed scaffold model, with a highly interconnected and gyroid-like porous structure (Fig. 1a and b). Using SEM, Fig. 1c, a smooth and regular surface was observed on PTMC scaffolds. However, on the surface of PTMC 20 and more importantly on PTMC 40 scaffolds, agglomerates of HA particles were observed, creating a topographical roughness on the surface of the built structures. The surface topography of PTMC 20 and PTMC 40 implants is relatively complex, with pores and undercuts associated with nano/micro-roughness, which are architectural prerequisites for *de novo* bone formation [24].

This difference of roughness and asperity was also noticeable using microCT (Fig. 1d). From the 3D reconstructions, the built internal architecture demonstrated a high degree of reproduction and homogeneity for the PTMC and PTMC 20 resins as seen in the cartography of the trabecular thickness (strut thickness) and trabecular space (pore diameter) (SF 1a and b respectively). The incorporation of 20 wt% of HA in the PTMC, resulted in a slight increase in the strut thickness (Fig. 1e and SF 1a) and a decrease of the average pore size (Fig. 1f and SF 1b) correlated with a decreased volume of porosity (Fig. 1g). These micro-architectural investigations revealed that the addition of 40 wt% of HA in PTMC resulted in a more heterogeneous structure with lower internal fidelity compared to the other resins. To conclude, by selecting an appropriate resin formulation and printing process, we were able to manufacture scaffolds with various amount of HA loaded into the PTMC, which exhibit reproducible macro- and microscopic features suitable for bone tissue engineering application [22].

SEM analyses performed on the surfaces of the SLA-fabricated scaffolds clearly showed a dense HA layer covering PTMC 20 (Fig. 2a and b) and PTMC 40 (data not shown). The needle-like nano-HA particles exhibit a random spatial alignment and

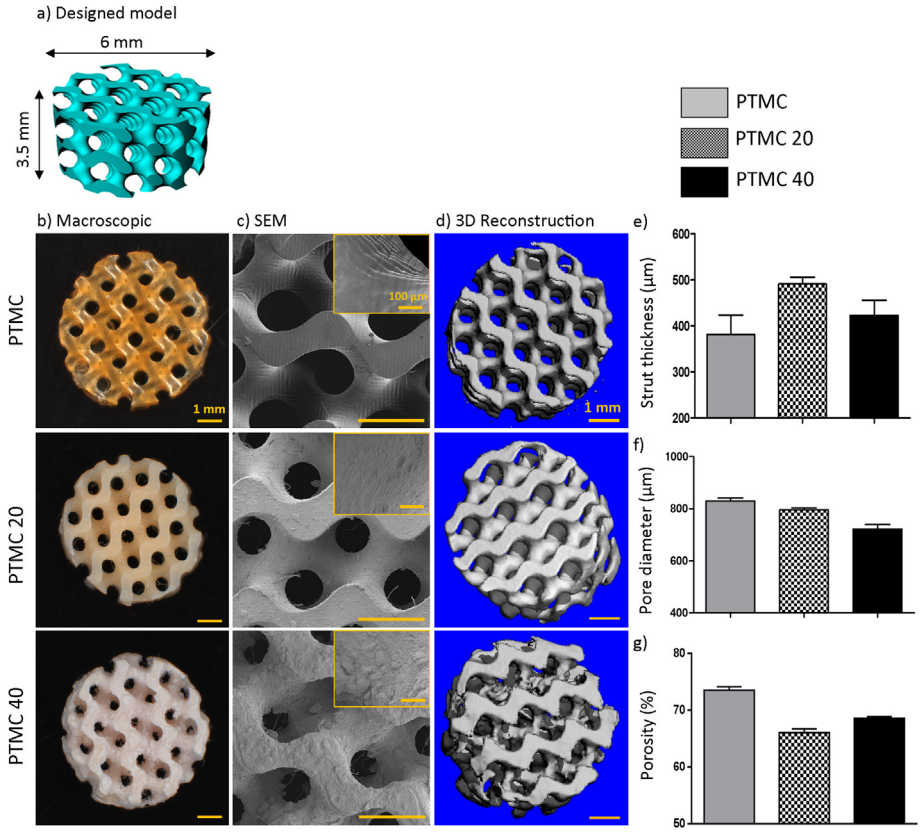

Fig. 1. Macroporous scaffolds of PTMC fabricated by stereolithography with varying amounts of HA. a) Model design processed using k3dsurf and Rhinoceros® software (exported as .STL-file, Standard tessellation language) and b) macroscopic and c) microscopic SEM observation of the different SLA-fabricated scaffolds (insets represent a magnification of the respective surfaces). CT monitoring of d) the 3D architecture and determination of e) the strut diameter, f) the pore diameter and g) the volume of porosity for PTMC, PTMC 20 and PTMC 40 scaffolds.

agglomeration, responsible for the singular topography previously described Fig. 1c and SF 2.

The spatial repartition of the HA particles was investigated on SEM using Backscattered electrons (BSE) mode, revealing a clear surface enrichment of Ca and P elements on PTMC 20 and PTMC 40 (Fig. 2c and d), with approximate thicknesses of 10 and 30 µm respectively. The quantitative analyses, Fig. 2e, demonstrated the global increase of Ca and P from PTMC 20 to PTMC 40 scaffolds, on both the bulk materials and the surfaces. However, significant enrichment of Ca and P elements was noted cortically, on both groups, in comparison to the bulk portion.

Importantly, the presence of C element (originating from polymeric matrix) apposed to Ca and P in the corralling layer suggests that HA nanoparticles are physically embedded in PTMC matrix and are not only loosely agglomerated.

Additionally, high resolution tomography, Fig. 2f, illustrated the formation of a thin and almost continuous microscale layer of tightly agglomerated HA nanoparticles on the disparate PTMC/HA scaffolds (which could not be observed using microCT 40 (SF 1) due to limitation of its resolution).

Subsequently, other physico-chemical characterizations were performed on PTMC/HA scaffolds in order to evaluate the additional changes triggered by HA incorporation. We noted that PTMC scaffolds tend to shrink following incubation in PBS, while PTMC 40 swells to 120% of its original size (Fig. 3a). This significant difference can be partly explained by the increased wettability of the structures containing high amount of HA, as shown by the contact angle measurement. An increasing load of HA was also correlated to an increasing protein surface adsorption (Fig. 3b), with dramatic augmentation for PTMC 40 compared to PTMC and PTMC 20. The presence of HA loaded in PTMC 20 and 40 allowed free Ca^{2+} to be continuously released *in vitro*. The main differences comparing both groups is the higher initial burst release of Ca^{2+} observed for PTMC 40 (Fig. 3c).

3.2. Cells proliferation and matrix deposition

The estimated number of cells per scaffold 1 day post-seeding, Fig. 4a, suggested that the addition of HA into the PTMC positively impacted the cells attachment to the scaffolds, as the DNA values significantly and gradually increased from pure PTMC to PTMC 40. Within 28 days of incubation all of the scaffolds permitted significant cell growth, as shown Fig. 4a and cells colonized the entire porous network of the scaffolds (Fig. 4c and d). However, considering the proliferation rate (taking into account the variation in the cell adhesion, Fig. 4a), we did observe that combining HA to PTMC resulted in a decelerated cell division (Fig. 4b). hBMSCs secreted a collagenous-rich matrix through the porosity of PTMC (data not shown) and PTMC 20 scaffolds (Fig. 4e). Histological observation revealed that cells proliferating in PTMC 40 scaffolds produced collagen as well, but in a reduced extend compared to PTMC and PTMC 20. Gene expression analysis corroborated this observation, as h-Col I gene was also found to be down-regulated following 14 days of cultivation, in both conditions, for PTMC 40 compared to PTMC and PTMC 20 (Fig. 4f).

3.3. hBMSCs osteogenic differentiation

The ALP activity was significantly increased for both PTMC 20 and PTMC 40 compared to PTMC surface from day 14 to day 21 in OM media (Fig. 5a). The presence of HA did influence the synthesis and the activity of ALP protein. Different tendencies could be

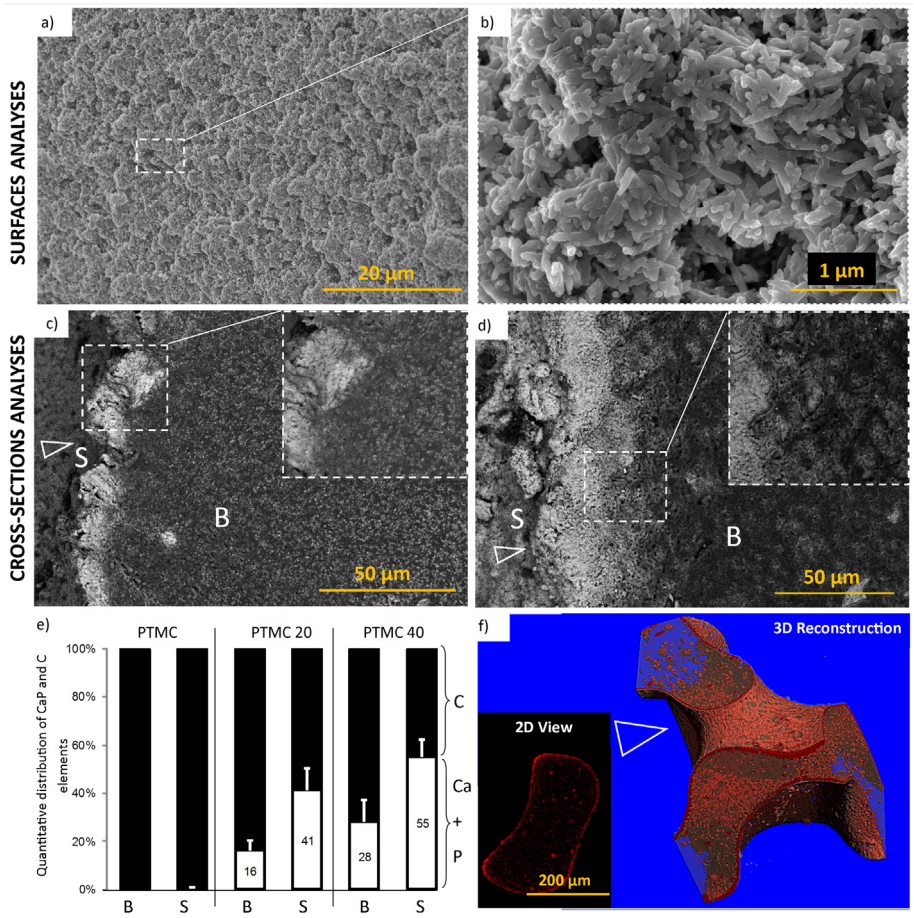

Fig. 2. Surface-enrichment of HA in PTMC scaffolds occurring during stereolithography processing. Illustration of the layer of agglomerated HA particles formed during SLA process covering the surface of the composite scaffolds, by SEM analysis of the surface (a and b, illustrating the random spatial organization of the needle-like shape HA nanoparticles on PTMC 20) and by BSE-SEM analysis performed on c) PTMC 20 and d) PTMC 40 (cross sections illustrating the presence of Ca + P (shown in light grey) dispersed in PTMC (C element is represented in dark grey)). e) Quantification of the Ca + P and C elements at the surface or in the bulk (S and B respectively) for the different scaffolds (measured on at least 6 different spectra) and f) high resolution microtomography reconstruction (illustrated only for PTMC 20), with high-contrasted area coloured in red (revealing HA-agglomerates repartition). White triangles point the dense HA-rich domains covering the scaffolds' surface.

observed from the investigation of the gene expression encoding for ALP. At day 14, h-ALP was significantly up-regulated only for PTMC 40 and not for PTMC 20. Indeed, h-ALP expression for PTMC 20 was similar to the control (PTMC scaffold without HA in BM condition, Fig. 5b), whereas ALP activity (corresponding to the activity of the protein synthesised) was shown to be significantly increased compared to PTMC only (Fig. 5a). Such discrepancy could reveal that ALP gene expression (which is an early marker for osteogenic differentiation) at day 14 for cell proliferating on PTMC 20 has already declined, as its peak, in terms of intensity of gene expression, precedes chronologically the peak of the encoded protein synthesis.

Calcium deposition was subsequently investigated using alizarin red staining (ARS) and quantification (Fig. 5c and d). The positive red staining revealed that the deposition of calcium increased over time in all surfaces, but more strongly on PTMC 20 and PTMC 40 after 28 days of incubation. The staining quantification confirmed the enhanced mineralisation on the films containing HA compared to the TCPS and PTMC surfaces at 28 days. Interestingly, higher ARS values were obtained on the PTMC 20 resin compared to the PTMC 40 for the two donors. Additionally, SEM observations, Fig. 5d, corroborated that hBMSCs mineralization was triggered by HA in PTMC, whereas a limited number of inorganic clusters (artificially coloured in red) could be distinguished on cell monolayers grown on PTMC and TCPS control surfaces.

3.4. In vivo bone formation

The SLA scaffolds were assessed using a calvarial defect model and bone ingrowth monitored using *in vivo* microCT at 0, 3 and 6 weeks with empty defects as control group. Selected scaffold architecture with a high degree of porosity (volume of porosity 70% and pore diameter of 700 ± 100 µm) showed to enable fast angiogenesis following implantation (Supplementary Fig. 3).

Bone ingrowth was observed after three weeks for all the groups and continued until week 6, with clear improvement for defects filled with PTMC 20 and 40 (Fig. 6a). As 6 mm large defect is considered to be non-critical size on rabbit calvarium model, small amount of new bone was formed for the empty groups but without reaching a full bridge over the 6 weeks of the experiment (Fig. 6a and b).

The quantification of new bone formation, Fig. 6b, showed additionally that scaffolds based on PTMC 40 significantly enhanced early bone tissue formation in the defect at week 3 and maintained higher bone content at week 6 compared to all the other groups. Noteworthy, PTMC 20 exhibited also a positive and significant effect on bone ingrowth, but only at 6 weeks compared to the empty defects. Histological analysis, Fig. 6c and d, showed that the majority of the tissue filling the defects was composed of soft tissue for the empty group and PTMC, with an estimated bone volume in the defect of only 26 and 38% respectively at 6 weeks. In

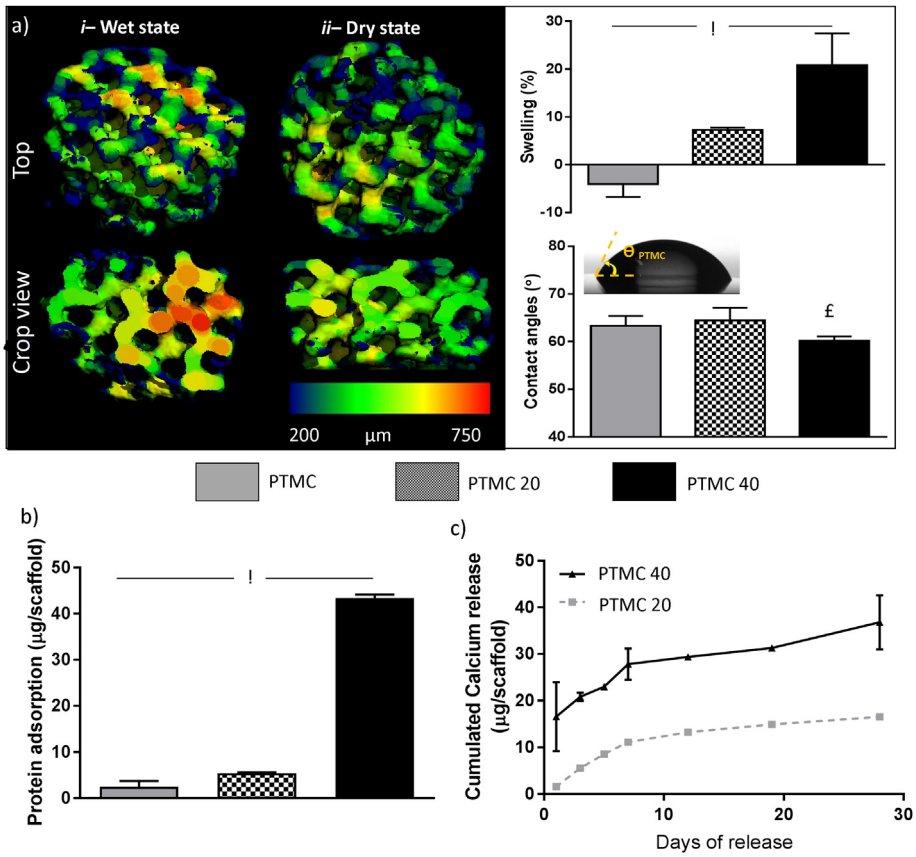

Fig. 3. Incorporating HA to PTMC scaffolds triggers fundamental physico-chemical alterations essential for promoting bone healing. a) Swelling behaviour illustrated by the cartography of the trabecular thickness distribution following 28 days of incubation in PBS i- before drying and ii- after drying (top view and crop view represented for PTMC 40), quantification of the swelling propensity for the different scaffolds correlated with the wettability (contact angle measurement) (! and £ indicate significance for the three groups or only for PTMC 40 respectively). b) Determination of protein absorption on the different scaffolds following 5 days of incubation in PBS-containing serum estimated using Bradford Protein assay (! indicates significance for the three groups). c) Analysis of the calcium release profile from the different scaffolds in PBS at 37 °C.

comparison, around 60% of the PTMC 20 and PTMC 40 scaffold porosities were filled by bone with no significant difference between both groups. By comparing both histological and microCT techniques, we can conclude that the amount of bone growing in PTMC 20 is not significantly different from PTMC 40 (Fig. 6d), but the bone seems more mineralized and mature in PTMC 40 (higher density values in microCT, Fig. 6b).

Injection of calcein green and xylenol orange fluorochromes after 2 and 4 weeks of implantation brought additional insight regarding the bone healing kinetic. Indeed, from the fluorescence staining, Fig. 7, two different bone ingrowth mechanisms are discernible depending on the scaffolds' composition. For the empty and PTMC groups, bone ingrowth started from the calvarial edges of the defect toward the center of the defect. In this study, bone deposition distribution was materialized by the sequential positioning of the fluorochromes, with a first green-stained front localized close to the edges of the defect, representing new bone formed at 2 weeks, and then a second red-stained front present in a more central area of the defect or of the PTMC scaffold for the new bone created at week 4. This phenomenon, corresponding to a distance osteogenesis [25], was observed in 100% of the histological sections (8 out of 8) for the PTMC group.

In opposition, adding HA into PTMC matrices directly influenced the bone healing cascade. Indeed, we observed a contact osteogenesis mechanism for PTMC 20 and PTMC 40, characterized by a direct bone apposition to the surface of the scaffolds growing toward the porous space compartment regardless the distance of the scaffold surface to the host bone bed (Fig. 7b and c) [25]. This pattern of new bone formation was observed in 5 (63%) and 8 (100%) out of 8 histological sections for PTMC 20 and PTMC 40 respectively. New bone was already formed at week 2 in the central part of PTMC 20 and, more importantly, of PTMC 40 scaffolds (depicted Fig. 7d by calcein green area quantification). PTMC scaffolds without HA allowed bone colonization, but mainly visible from the peripheral areas, following 4 weeks of implantation, Fig. 7b, c and d.

When looking closely at the interface between the surface of the biomaterials and the neo-formed tissue (bone-bonding), we observed unequivocally a significant improvement regarding the osseointegration of the scaffolds containing 40 wt% HA compared to PTMC with 20 wt% HA (Fig. 7e). Indeed, the degree of bone anchorage to the scaffolds was enhanced by a factor 1.4 for PTMC 40 compared to PTMC 20, meaning that an average of 60 to 80% of the surface of the PTMC 40 scaffolds were in direct contact with newly formed bone. Finally, a higher degree of bone tissue maturity was achieved in the porous network of PTMC 20 and PTMC 40, with marrow spaces and an intense vascularization, in comparison to PTMC scaffolds (SF 3).

4. Discussion

4.1. Biological response of the disparate PTMC/HA scaffolds

Naturally, bone healing cascade is initiated by the migration and then the differentiation of progenitor osteogenic cell

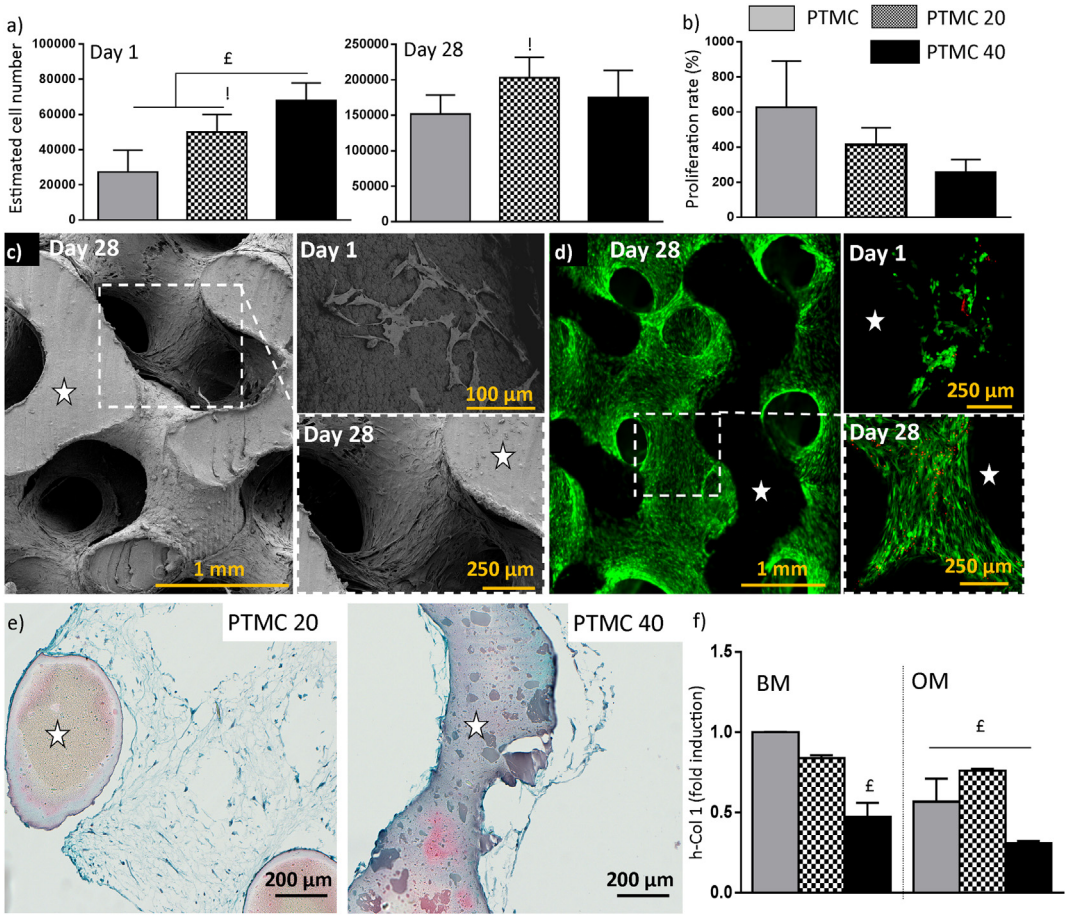

Fig. 4. Loading HA in PTMC scaffold impacts *in vitro* cell adhesion, proliferation and matrix deposition. a) Estimation of scaffolds colonization by hBMSCs from day 1 to day 28 (estimated by DNA assay quantification, hBMSCs having approximately 10.5 pg of DNA per cell, ! and £ reported significance for PTMC 20 and PTMC 40 respectively compared to PTMC) and b) representation of the proliferation rate for the different scaffolds. c) SEM observation and d) Live/Dead® staining of scaffold's cross-section at 1 and 28 days post-seeding (illustration for PTMC 20, from z-stack acquisitions at 2.5 X and 10 X). e) Histological Safranin-O Fast Green staining illustrating in blue the collagen fibres present in the ECM deposited by hBMSCs after 28 days of cultivation in OM (showed for PTMC 20 and PTMC 40, at 10 X.). f) Type I human collagen gene expression analysed after 14 days of hBMSCs cultivation on the different scaffolds in basal and osteogenic media (BM and OM respectively, £ reported significance compared to PTMC in BM). White stars present in c, d and e denote scaffold's cross-section.

population [26]. Therefore, it is essential to investigate the influence of scaffold's properties on those earliest biological events. In order to mimic such *in vivo* phenomenon, human primary stem cells isolated from bone marrow compartment were employed for the *in vitro* adhesion, proliferation and osteogenic differentiation investigations.

The *in vitro* attachment study showed that PTMC 40 allowed more robust cell adhesion compared to PTMC and PTMC 20 (Fig. 4). The modification of the cell adhesion parameter is likely to result from the topographical and chemical surface alteration observed on PTMC 40 surfaces (SF 2). Being able to modulate this parameter by varying HA content could have triggered the positive bone healing outcomes observed in PTMC/HA, as several authors demonstrated that osteoprogenitor cells start to attach and to colonize biomaterial scaffolds within one day of implantation [27,28]. Interestingly, the proliferation rate over 28 days of culture was the lowest in this same PTMC 40 group. In fact, it was largely reported that surface roughness negatively impacts cell proliferation, which correlates to a more differentiated osteogenic cell phenotype [28]. Our findings corroborate this hypothesis, as the *in vitro* osteogenic markers (ALP and mineralization) were increased in PTMC containing HA compared to pure PTMC (Fig. 5). Surprisingly, both collagen deposition along with type I collagen gene regulation were decreased in PTMC 40 compared to PTMC and PTMC 20. However, this is not an isolated finding, as other publications have observed that osteogenic differentiation of MSCs in ceramics did not always result in Col-I gene upregulation [29]. Chronologically, the matrix secreted by osteogenic cells during *de novo* endosseous implant healing is composed of non-collagenous proteins (called cement line [24]), which could explain the difference observed *in vitro* between PTMC and PTMC 40 (Fig. 4).

Following implantation of composite PTMC scaffolds in rabbit calvarial defect model, a significant amount of new bone ingrowth through the entire porosity of the PTMC 20 and PTMC 40 scaffolds was observed. In comparison, mainly soft tissue was detected in the control PTMC group. In terms of quantification of new bone formation, PTMC 20 performed as well as PTMC 40, but the osseointegration quality of the implants (looking at the focal interaction between the biomaterials and the tissue) correlated with the highest amount of HA.

Noteworthy, the kinetic of new bone ingrowth *in vivo* investigated using fluorochromes staining revealed that the amount of HA into the PTMC matrix directly governed the osteogenesis mechanism (Fig. 7).

De novo bone formation was detected on the surface of PTMC 20 and more importantly, on PTMC 40, due to the osteoconductivity of the composite scaffolds.

In comparison, bone formation for PTMC only resulted exclusively from distance osteogenesis, starting from the edges of the calvarial defect toward the center. In implantology, contact

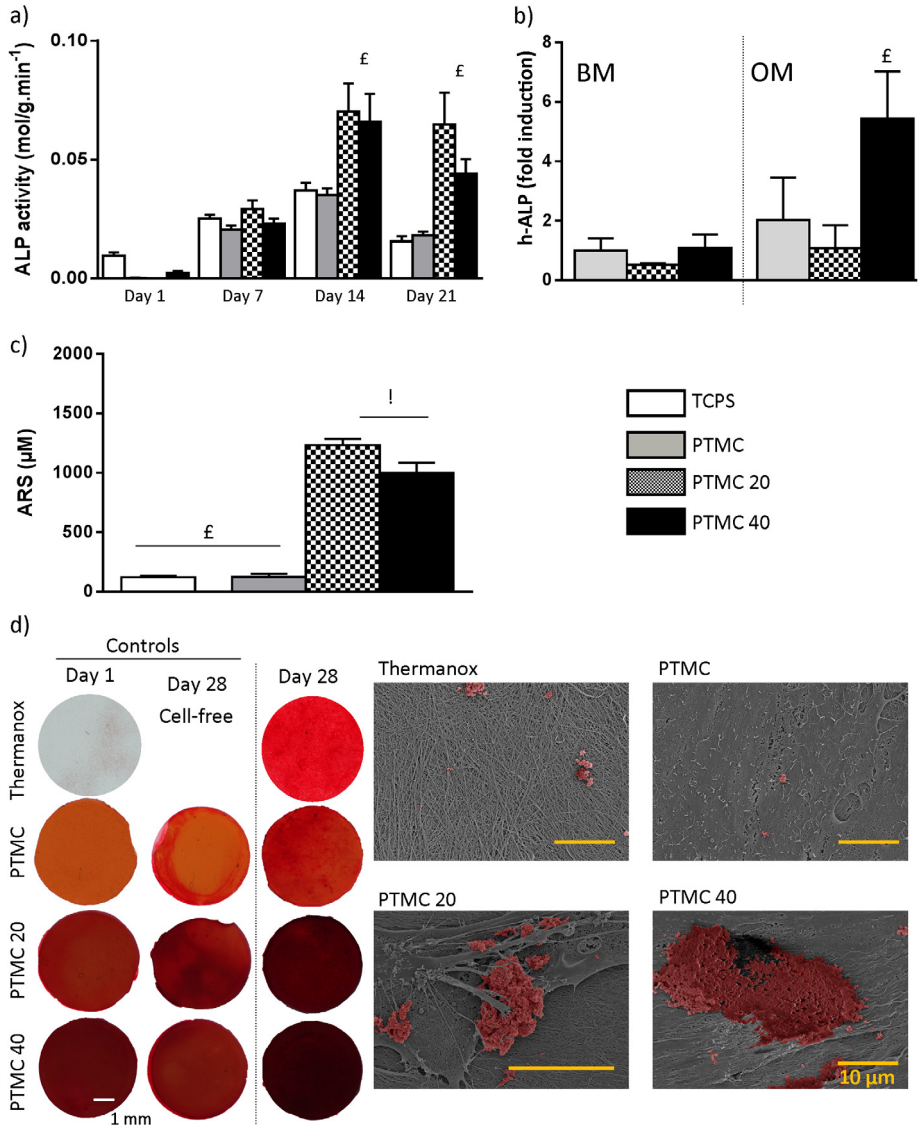

Fig. 5. Combining HA to PTMC exacerbates osteogenic differentiation of hBMSCs under OM condition. Influence of PTMC scaffold composition on a) ALP activity, b) h-ALP gene expression (analysed after 14 days of hBMSCs cultivation on the different scaffolds in basal and osteogenic media (BM and OM respectively), £ reported significance compared to PTMC) and c) Alizarin Red Staining (ARS) quantification at day 28 (with £ indicating significance between PTMC/HA and controls and ! indicating significance between PTMC 20 and PTMC 40) (ARS corrected by the background O.D. values due to the composition of the films at day 1) (a and c represent average values ±standard error of the mean). d) Illustration of the intensity of ARS for the different controls and film materials and of calcium deposition on the cell monolayer following 28 days of cultivation on the different surfaces (SEM images with mineralization highlighted by artificial red colouring using Photoshop®). (For interpretation of the references to colour in this figure legend, the reader is referred to the web version of this article.)

osteogenesis is the result of an implant allowing for "osteoconduction", meaning that its surface favours osteogenic cells to migrate and to attach to its surface (importance of fibrin clot and implant micro-topography as previously mentioned). Next in order, a new mineralized tissue similar to a cement line (occurring naturally in bone fracture healing) is formed at the interface implant/tissue, which is called "*de novo* bone" formation. To summarize, the main differences between contact osteogenesis and distance osteogenesis is the formation of the cement line ("*de novo* bone formation") covering directly the surface of the implant in the first scenario.

Those different osteogenesis mechanisms, extensively described by Davies et al. [25,30,31], have a direct impact on the quality of implant endosseous integration (as seen Fig. 7e).

Indeed, as observed by Puelo *et al.*, bone growing rate occurring through contact osteogenesis is 30% faster than in distance osteogenesis [32]. Our findings corroborate this phenomenon, as we clearly noted, Fig. 7d, more bone formed at 2 and 4 weeks in PTMC 40 (either in the periphery or in the center of the defect).

4.2. Correlation between PTMC/HA fabrication process and biological properties

In order to unravel underlying mechanisms toward biofunctionality of the scaffolds, several physico-chemical characterizations of the scaffolds have been undertaken. Importantly, increasing the volume fraction of HA particles loaded into the PTMC resin resulted in a dense CaP cortical layer, observed on the surface of the composite stereolithography scaffolds (Fig. 2). Indeed, it is known that the stability and segregation of nanoparticles in a polymer/solvent mixture is governed by the nature of the interactions between the blend and the particles (Van Der Waals, electrostatic, hydrophobic-hydrophilic, *etc.*).

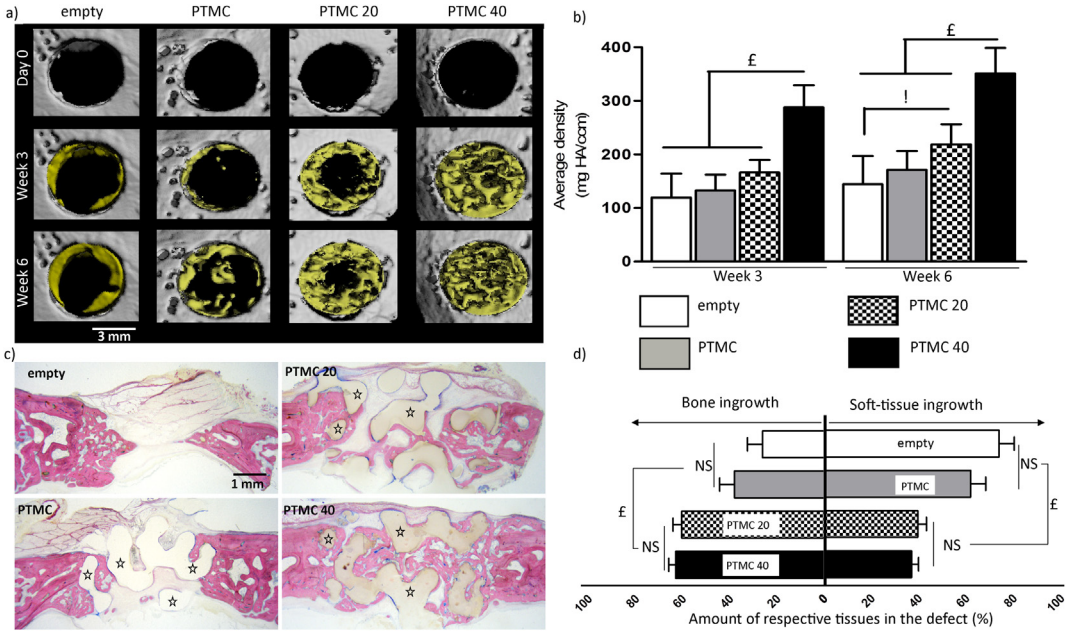

Fig. 6. PTMC/HA stimulates *in vivo* mineralization and bone formation. a) Representative 3D reconstructions from the microCT images showing the native calvarial bone (in grey) and the new bone (in yellow) (the intrinsic signals of the scaffolds were subtracted for all the time points). b) Quantification of the new bone formation at week 3 and 6 estimated by the average density of the defects (corrected by the postoperative values due to the intrinsic signal of the scaffolds (day 0), with ! and £ indicating significance compared to PTMC 20 and 40 respectively). c) Giemsa-Eosin staining revealing the new bone formation after 6 weeks of implantation (bone is stained in pink and soft tissue appeared in slight brown, stars denote scaffolds' cross-section) and d) histomorphometric semi-quantification of bone versus soft tissue in the defect for the different groups (£ indicated significance compared to PTMC 20 and 40). (For interpretation of the references to colour in this figure legend, the reader is referred to the web version of this article.)

In the selected stereolithography fabrication process, the nature of the polymeric phase evolved from soluble macromers of PTMC-MA to photo-crosslinked chains of PTMC. This chemical modification directly impacts on the polymer's radius of gyration and its chain stretchability. Taking into consideration that spatial distribution of nanoparticles can be controlled depending on the size of the nanoparticles relative to the radius of gyration of the polymer [17], we hypothesise that a fraction of HA particles are expelled to the surfaces during/after the photo-crosslinking reaction. Additionally, as more crosslinks are formed in the polymer network during photoreaction, conformational entropy in the system naturally decreases. To regain a certain degree of entropy (and in this way polymer chains do not have to stretch around nanoparticles), the flexible polymer chains can expulse larger particles at the surface, which is one of the thermodynamic mechanisms behind some of the self-healing [33], solar cells [34] or optically-advanced nanocomposite materials [35]. This "depletion attraction" phenomenon allows for manipulation of particles to self-localize in specific regions of the material interfaces [33]. The time interval between each layer formation employed in the stereolithography process (*i.e.* 9 seconds) might not be long enough to allow for HA segregation at the interface between every layer. This could be the reason why HA enrichment was only observed at the surface of the SLA-fabricated scaffolds but not between every layer of the photo-crosslinked material.

Additionally, during the purification process, the SLA-fabricated scaffolds (initially soaked in propylene carbonate) undergo a solvent exchange using ethanol (as non-solvent) followed by a drying step. This solvent exchange is responsible for a swelling and then a deswelling of the materials, which could potentially trigger particles migration from the polymer network at the non-solvent/polymer interface, resulting in a corral-like spatial enrichment of the particles [17].

CaP mineral deposition is commonly performed to endow 3D-printed structures with osteogenic properties [14,36,37]. Nevertheless, the reported processes exhibit intrinsically several limitations, regarding for example the numerous post-printing steps required to create this mineral deposition. In addition, there is a limited physical integrity of the CaP deposited on the printed materials with risk of layer delamination and particle loosening. In this study, the HA enrichment observed on the SLA-fabricated PTMC/HA scaffolds did not require additional steps compared to the fabrication of PTMC only. Of importance, the HA particles are fully integrated in the polymer matrix (as shown Fig. 2 with the high amount of "C" element at the surface, originating from the PTMC matrix) conferring physical stability without risk of layer delamination and particle loosening.

Additionally, we observed different behaviour in terms of swelling of PTMC/HA which could only be partly attributed to the increased wettability of the structures containing high amount of HA (Fig. 3a). However, other parameters, such as *i*- the density of crosslinking into the PTMC matrices which can be altered by the presence of HA, or *ii*- the presence of HA in the bulk of the materials, can also influence the propensity of the photo-crosslinked scaffolds to swell, without having a direct impact on its wettability. For the protein adsorption study, we selected a medium with 10% of serum that naturally contains a mixture of proteins/growth factors as a model. We observed that PTMC 40 propensity to swell and also to adsorb proteins was significantly increased compared to the other groups. Those physico-chemical characteristics have a tremendous impact on bone healing, as several proteins have been shown to trigger cells recruitment, binding and differentiation [38], such as growth factors (e.g. BMPs, PDGF, TGF-b, *etc.*) but also platelet releasate and fibrinogen [25]. A surface that can bind more circulating proteins and formed quickly a fibrin clot will favour osteogenic cells (and platelets) to migrate through this transitory matrix, releasing in turn other cytokines and bone growth factors. By reaching the surface, bone cells will be able to synthetise *de novo* bone on the implant surface itself.

This finding explains as well the significant enhancement of hBMSCs attachment witnessed on scaffolds containing 40 wt% HA (Fig. 4a).

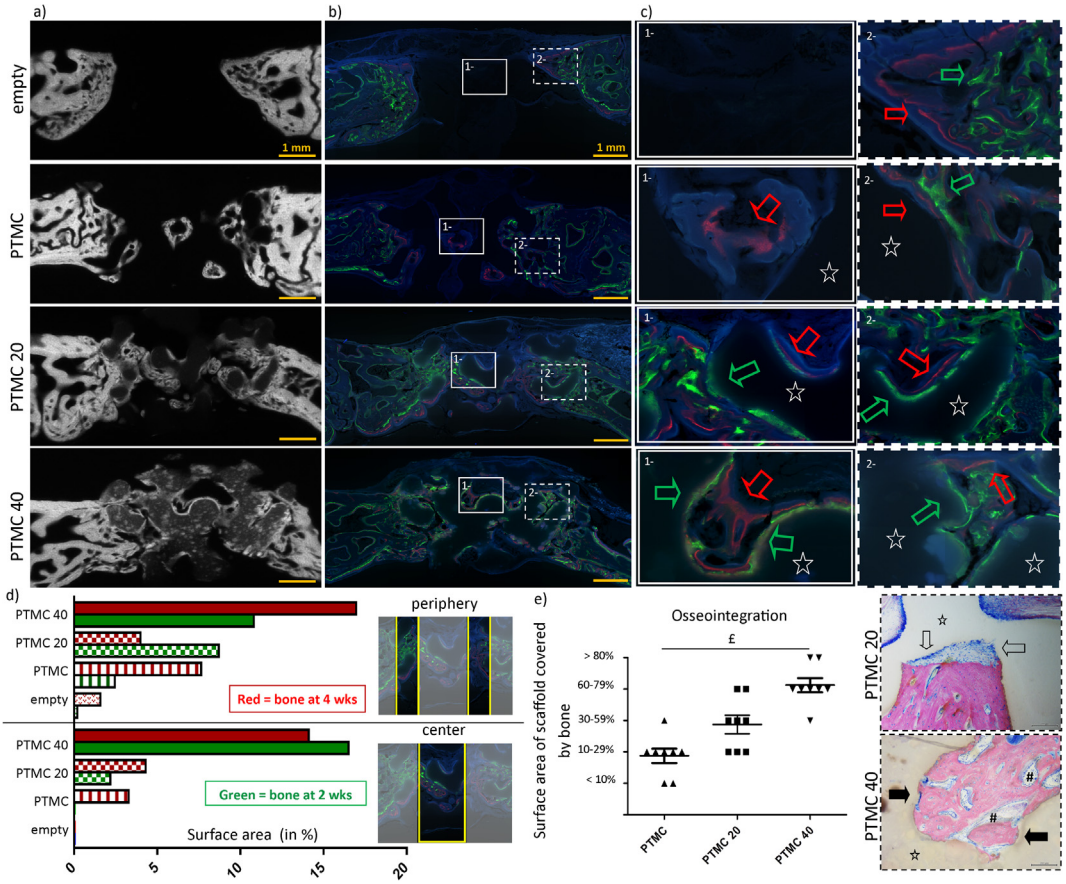

Fig. 7. Osteoconductive HA directly governs PTMC composite implants osseointegration by contact osteogenesis and de novo bone formation. a) Contact radiographs of the defects correlated with b) fluorescence imaging of new bone formed following 2 weeks (in green) and 4 weeks (in red) of implantation. c) High magnification micrographs of 1- central and 2- peripheral regions of the defect highlighting the different osteogenesis mechanisms (i.e. distance osteogenesis versus contact osteogenesis observed for PTMC and PTMC/HA respectively). Stars denoted the biomaterial cross-sections, green and red arrows represented the bone formed after calcein green and xylenol orange injection respectively. d) Zonal histomorphometric illustration of bone healing kinetic by quantification of green-labelled and red/orange-labelled areas (representing new bone formed at 2 and 4 weeks respectively in the central and peripheral area (each of 7.7 mm^2, expressed in percentage relative to the available porous space) of the images represented Fig. 6b, using Photoshop®, n = 1/group). e) Representation of different degree of bone-bonding scaffolds with semi-quantitative histomorphometric estimation of the degree of scaffold anchorage to the newly formed bone (£ indicated significance between the three groups, n = 8/group). Stars denote scaffold biomaterials, empty arrows show surface biomaterial in contact with soft tissue whereas black arrows depict direct bone integration, hashtags point out the marrow tissue. (For interpretation of the references to colour in this figure legend, the reader is referred to the web version of this article.)

Additionally, the increased bioactivity of the CaP loaded PTMC could be also attributed to the higher amount of Ca^{2+} released, Fig. 3c. A major criterion of osteoconductive CaP-based biomaterials relies in their ability to release free calcium in their microenvironment [21,39]. Under normal condition, extracellular fluids are already supersaturated, but peri-prosthetic acidification happening during bone formation and remodelling (due to macrophages and osteoclasts activity) permits Ca^{2+} and phosphate ions dissolution and leads to the precipitation of carbonate hydroxyapatite layer (CHA) at the surface of the implant [38]. Additionally, Ca^{2+} released influences also the fate of osteoprogenitor cells in terms of adhesion, proliferation and differentiation [40,41], which finally triggers the biomineralization cascade.

In this study, we purposely selected un-sintered HA (containing more soluble calcium phosphate ions and an increased surface area), as sintered HA has been reported to resorb too slowly, which can provoke long-term complications [41]. Secondly, the surface-enrichment of HA particles observed in PTMC 20 and PTMC 40 may facilitate Ca^{2+} dissolution and diffusion compared to homologues where CaP would be physically entrapped in crosslinked hydrophobic polymer matrices.

Several investigations have shown that the amount of HA exposed at the surface of composite scaffolds is of critical importance for neo-bone formation. As instance, Zhao *et al.* developed composite scaffolds (bioactive glass with polymers poly(3-hydroxy butyrate-co-3-hydroxyhexanoate) (PHBHHx)) using 3D Bioplotter system. *In vivo* experiments revealed that more bone was formed in Bioglass/polymer composites, but that even in the group containing high amount of Bioglass (polymer/bioactive glass ratio of 1/7 w/w), the early bone deposition (at 3 weeks) was not in direct contact with the material surface, but was following a distance osteogenesis mechanism, similarly to the Bioglass-free scaffolds. They mentioned that the evaporation step included in the fabrication process was responsible to the creation of a thin polymeric layer covering the surface and the bioactive particles of the composite scaffold, which can have a direct impact on bone formation [42]. Similar new bone formation kinetic "*extending from the edges of the defects towards the center of the defects*" was mentioned by another recent work from Zeng *et al.* using PTMC doped with TCP (β-tricalcium phosphate) or BCP (biphasic calcium phosphate), produced by salt-leaching technique [43]. Finally, using similar needle-shaped HA nanoparticles, Barbieri *et al.* demonstrated that only PDLLA composite scaffold with 40% weight HA (made by salt-leaching) could trigger ectopic bone formation, due to the highest amount of HA exposed at the surface of the scaffolds (impacting Ca^{2+} release, surface topography, protein adsorption, *etc.*), com-

pared to scaffolds containing 10 or 20% of CaP [21]. Those are few examples showing that exposing HA to the surface of 3D printed constructs could favour osseointegration of the biomaterials. Nevertheless, no report on similar self-corralling HA composite scaffolds have been presented so far, which opens great avenues in the field of bioactive scaffolds. Additionally, the influence of the nanoparticle shape on this segregation behaviour would definitely deserve more investigation, as other parameters such as particles concentration and size have been shown to influence polymer/-nanoparticle blends' behaviour [44].

Finally, one of the singularities of the PTMC matrix degradation in opposition to the hydrolytic degradation of the polyesters, is the surface erosion mechanism [11]. The long-term success of any biomaterial-based tissue engineering strategy depends greatly on an appropriate degradation kinetic. Frequent failure attempts have been reported due to unsuitable scaffold resorption rates [45]. *In vitro* investigations have already demonstrated that photo-crosslinked PTMC is erodible, but at a rate significantly reduced compared to non-crosslinked PTMC (*e.g.* in cholesterol esterase solution, ±2200 versus ±20 $\mu g/cm^2 \times$ day for PTMC and for photo-crosslinked PTMC respectively [46]). In our 6 weeks *in vivo* study, no evident sign of biomaterial degradation was observed and longer-term implantation period is required to specifically investigate PTMC degradation. Alternative copolymers, based on reported poly(TMC-*co*-CL) [47] or poly(TMC-*co*-DLLA) [48] could help in accelerating the biodegradation of the construct.

5. Conclusion

Material-directed endosseous integration is commonly obtained by combining macroporous scaffolds with osteogenic growth factors or with stem cells. Alternatively, emerging trends in the field of bone repair have paid more attention to the hierarchical fabrication of macro/microstructural designs of composite ceramic-polymer matrices, allowing to render those biomaterials osteopromotive.

We report on the fabrication of a scaffold made of poly(trimethylene carbonate) doped with hydroxyapatite nanoparticles for bone tissue engineering using stereolithography. Of interest, the SLA-process leads to a surface-enrichment of the HA in the composite PTMC/HA scaffolds. *In vitro* and *in vivo* experiments revealed the importance of microscale-structured PTMC/HA scaffolds for bone tissue engineering and how phase enrichment can potentially be used advantageously.

As perspective, optimisation of the interactions between nanoparticles and polymers in composite structures in combination with the stereolithography process could permit to engineer hierarchically ordered biomaterials with decreased loading of bioactive cues (*i.e.* nanoscopic HA) that exhibit tailored architecture and functionalities.

More generally, the possibility to control multiple length scales and dimensions could have remarkable applications in the burgeoning field of additive manufacturing systems.

Acknowledgment

Authors would like to acknowledge NSFC-DG-RTD Joint Scheme (Project No. 51361130034) and the European Union's 7th Framework Program under Grant agreement n° NMP3-SL-2013-604517, Project RAPIDOS. Additionally, we are grateful to the membres of the preclinical facility (Zeiter S., Kluge K., Eberli, U. and Schmidt T.) and to Nehrbass D. for technical and histological assistance. Furthermore the authors express their gratitude to Dr. Davide Barbieri and Mr. Rongquan Duan in Xpand Biotechnology BV for supplying hydroxyapatite nanoparticles.

Appendix A. Supplementary data

Supplementary data associated with this article can be found, in the online version, at http://dx.doi.org/10.1016/j.actbio.2017.03.006.

References

[1] P.V. Giannoudis, H. Dinopoulos, E. Tsiridis, Bone substitutes: an update, Injury 36 (Suppl. 3) (2005) S20–S27.
[2] S. Bose, S. Vahabzadeh, A. Bandyopadhyay, Bone tissue engineering using 3D printing, Mater. Today 16 (2013) 496–504.
[3] C.W. Hull. Apparatus for production of three-dimensional objects by stereolithography. 1986.
[4] S. Schuller-Ravoo, E. Zant, J. Feijen, D.W. Grijpma, Preparation of a designed poly(trimethylene carbonate) microvascular network by stereolithography, Adv. Healthcare Mater. 3 (2014) 2004–2011.
[5] M.A. Geven, D. Barbieri, H. Yuan, J.D. de Bruijn, D.W. Grijpma, Preparation and mechanical properties of photo-crosslinked poly(trimethylene carbonate) and nano-hydroxyapatite composites, Clin. Hemorheol. Microcirc. 60 (2015) 3–11.
[6] M.A. Geven, V. Varjas, L. Kamer, X. Wang, J. Peng, D. Eglin, D.W. Grijpma, Fabrication of patient specific composite orbital floor implants by stereolithography, Polym. Adv. Technol. 26 (2015) 1433–1438.
[7] K. Fukushima, Poly(trimethylene carbonate)-based polymers engineered for biodegradable functional biomaterials, Biomater. Sci. 4 (2015) 9–24.
[8] P. Gentile, V. Chiono, I. Carmagnola, P.V. Hatton, An overview of poly(lactic-co-glycolic) acid (PLGA)-based biomaterials for bone tissue engineering, Int. J. Mol. Sci. 15 (2014) 3640–3659.
[9] M.S. Taylor, A.U. Daniels, K.P. Andriano, J. Heller, Six bioabsorbable polymers: in vitro acute toxicity of accumulated degradation products, J. Appl. Biomater. 5 (1994) 151–157.
[10] A.A. Ignatius, O. Betz, P. Augat, L.E. Claes, In vivo investigations on composites made of resorbable ceramics and poly(lactide) used as bone graft substitutes, J. Biomed. Mater. Res. 58 (2001) 701–709.
[11] Z. Zhang, R. Kuijer, S.K. Bulstra, D.W. Grijpma, J. Feijen, The in vivo and in vitro degradation behavior of poly(trimethylene carbonate), Biomaterials 27 (2006) 1741–1748.
[12] A.P. Pêgo, A.A. Poot, D.W. Grijpma, J. Feijen, In vitro degradation of trimethylene carbonate based (Co)polymers, Macromol. Biosci. 2 (2002) 411–419.
[13] E. Bat, Z. Zhang, J. Feijen, D.W. Grijpma, A.A. Poot, Biodegradable elastomers for biomedical applications and regenerative medicine, Regen. Med. 9 (2014) 385–398.
[14] M. Dadsetan, T. Guda, M.B. Runge, D. Mijares, R.Z. LeGeros, J.P. LeGeros, D.T. Silliman, L. Lu, J.C. Wenke, P.R. Brown Baer, M.J. Yaszemski, Effect of calcium phosphate coating and rhBMP-2 on bone regeneration in rabbit calvaria using poly(propylene fumarate) scaffolds, Acta Biomater. 18 (2015) 9–20.
[15] J.W. Lee, K.S. Kang, S.H. Lee, J.Y. Kim, B.K. Lee, D.W. Cho, Bone regeneration using a microstereolithography-produced customized poly(propylene fumarate)/diethyl fumarate photopolymer 3D scaffold incorporating BMP-2 loaded PLGA microspheres, Biomaterials 32 (2011) 744–752.
[16] C.B. Danoux, D. Barbieri, H. Yuan, J.D. de Bruijn, C.A. van Blitterswijk, P. Habibovic, In vitro and in vivo bioactivity assessment of a polylactic acid/hydroxyapatite composite for bone regeneration, Biomatter 4 (2014) e27664.
[17] A.C. Balazs, T. Emrick, T.P. Russell, Nanoparticle polymer composites: where two small worlds meet, Science 314 (2006) 1107–1110.
[18] L.A. Renna, C.J. Boyle, T.S. Gehan, D. Venkataraman, Polymer nanoparticle assemblies: a versatile route to functional mesostructures, Macromolecules 48 (2015) 6353–6368.
[19] M.E. Mackay, A. Tuteja, P.M. Duxbury, C.J. Hawker, B. Van Horn, Z. Guan, G. Chen, R.S. Krishnan, General strategies for nanoparticle dispersion, Science 311 (2006) 1740–1743.
[20] N. Jouault, D. Zhao, S.K. Kumar, Role of casting solvent on nanoparticle dispersion in polymer nanocomposites, Macromolecules 47 (2014) 5246–5255.
[21] D. Barbieri, A.J. Renard, J.D. de Bruijn, H. Yuan, Heterotopic bone formation by nano-apatite containing poly(D, L-lactide) composites, Eur. Cell Mater. 19 (2010) 252–261.
[22] V. Karageorgiou, D. Kaplan, Porosity of 3D biomaterial scaffolds and osteogenesis, Biomaterials 26 (2005) 5474–5491.
[23] M. Herrmann, J.J. Bara, C.M. Sprecher, U. Menzel, J.M. Jalowiec, R. Osinga, A. Scherberich, M. Alini, S. Verrier, Pericyte plasticity – comparative investigation of the angiogenic and multilineage potential of pericytes from different human tissues, Eur. Cell Mater. 31 (2016) 236–249.
[24] P.R. Kuzyk, E.H. Schemitsch, The basic science of peri-implant bone healing, Indian J. Orthop. 45 (2011) 108–115.
[25] J.E. Davies, Understanding peri-implant endosseous healing, J. Dent. Educ. 67 (2003) 932–949.
[26] J.E. Davies, In vitro modeling of the bone/implant interface, Anat. Rec. 245 (1996) 426–445.
[27] U. Meyer, U. Joos, J. Mythili, T. Stamm, A. Hohoff, T. Fillies, U. Stratmann, H.P. Wiesmann, Ultrastructural characterization of the implant/bone interface of immediately loaded dental implants, Biomaterials 25 (2004) 1959–1967.

[28] M. Ramazanoglu, Y. Oshida, Osseointegration and bioscience of implant surfaces – current concepts at bone-implant interface, in: P.I. Turkyilmaz (Ed.), Implant Dentistry – A Rapidly Evolving Practice, INTECH, 2011.
[29] H. Yuan, H. Fernandes, P. Habibovic, J. de Boer, A.M. Barradas, A. de Ruiter, W.R. Walsh, C.A. van Blitterswijk, J.D. de Bruijn, Osteoinductive ceramics as a synthetic alternative to autologous bone grafting, Proc. Natl. Acad. Sci. U.S.A. 107 (2010) 13614–13619.
[30] J.E. Davies, Mechanisms of endosseous integration, Int. J. Prosthodont 11 (1998) 391–401.
[31] J.E. Davies, Bone bonding at natural and biomaterial surfaces, Biomaterials 28 (2007) 5058–5067.
[32] D.A. Puleo, A. Nanci, Understanding and controlling the bone-implant interface, Biomaterials 20 (1999) 2311–2321.
[33] J.Y. Lee, G.A. Buxton, A.C. Balazs, Using nanoparticles to create self-healing composites, J. Chem. Phys. 121 (2004) 5531–5540.
[34] K.M. Coakley, M.D. McGehee, Conjugated polymer photovoltaic cells, Chem. Mater. 16 (2004) 4533–4542.
[35] Y. Lin, A. Boker, J. He, K. Sill, H. Xiang, C. Abetz, X. Li, J. Wang, T. Emrick, S. Long, Q. Wang, A. Balazs, T.P. Russell, Self-directed self-assembly of nanoparticle/copolymer mixtures, Nature 434 (2005) 55–59.
[36] P.X. Lan, J.W. Lee, Y.J. Seol, D.W. Cho, Development of 3D PPF/DEF scaffolds using micro-stereolithography and surface modification, J. Mater. Sci. – Mater. Med. 20 (2009) 271–279.
[37] V. Luangphakdy, E. Walker, K. Shinohara, H. Pan, T. Hefferan, T.W. Bauer, L. Stockdale, S. Saini, M. Dadsetan, M.B. Runge, A. Vasanji, L. Griffith, M. Yaszemski, G.F. Muschler, Evaluation of osteoconductive scaffolds in the canine femoral multi-defect model, Tissue Eng. Part A 19 (2013) 634–648.
[38] R.Z. LeGeros, Calcium phosphate-based osteoinductive materials, Chem. Rev. 108 (2008) 4742–4753.
[39] D.S. Metsger, R.M. DePhilip, T.G. Hayes, An autoradiographic study of calcium phosphate ceramic bone implants in turkeys, Clin. Orthop. Relat. Res. (1993) 283–294.
[40] P. Ducheyne, Q. Qiu, Bioactive ceramics: the effect of surface reactivity on bone formation and bone cell function, Biomaterials 20 (1999) 2287–2303.
[41] M. Bohner, L. Galea, N. Doebelin, Calcium phosphate bone graft substitutes: failures and hopes, J. Eur. Ceram. Soc. 32 (2012) 2663–2671.
[42] S. Zhao, M. Zhu, J. Zhang, Y. Zhang, Z. Liu, Y. Zhu, C. Zhang, Three dimensionally printed mesoporous bioactive glass and poly(3-hydroxybutyrate-co-3-hydroxyhexanoate) composite scaffolds for bone regeneration, J. Mater. Chem. B 2 (2014) 6106–6118.
[43] N. Zeng, A.C. van Leeuwen, D.W. Grijpma, R.R. Bos, R. Kuijer, Poly(trimethylene carbonate)-based composite materials for reconstruction of critical-sized cranial bone defects in sheep, J. Craniomaxillofac. Surg. (2016).
[44] E.S. McGarrity, A.L. Frischknecht, M.E. Mackay, Phase behavior of polymer/nanoparticle blends near a substrate, J. Chem. Phys. 128 (2008) 154904.
[45] B.D. Ulery, L.S. Nair, C.T. Laurencin, Biomedical applications of biodegradable polymers, J. Polym. Sci. B Polym. Phys. 49 (2011) 832–864.
[46] E. Bat, T.G. van Kooten, J. Feijen, D.W. Grijpma, Resorbable elastomeric networks prepared by photocrosslinking of high-molecular-weight poly (trimethylene carbonate) with photoinitiators and poly(trimethylene carbonate) macromers as crosslinking aids, Acta Biomater. 7 (2011) 1939–1948.
[47] D.W. Grijpma, Q. Hou, J. Feijen, Preparation of biodegradable networks by photo-crosslinking lactide, epsilon-caprolactone and trimethylene carbonate-based oligomers functionalized with fumaric acid monoethyl ester, Biomaterials 26 (2005) 2795–2802.
[48] S. Sharifi, D.W. Grijpma, Resilient amorphous networks prepared by photo-crosslinking high-molecular-weight D, L-lactide and trimethylene carbonate macromers: mechanical properties and shape-memory behavior, Macromol. Biosci. 12 (2012) 1423–1435.